Computers and Structures 329 (2026) 108251

Contents lists available at ScienceDirect

Computers and Structures

journal homepage: www.elsevier.com/locate/compstruc

Stress-field reconstruction from laser interferometric strain measurements☆

Alessandro Menghini [a], Hasan Ceylan [a], Alper Kanyilmaz [a,*], Simone Donadello [b], Cecilia Clivati [b], Daniele Loiacono [c]

[a] Department of Architecture, Built Environment and Construction Engineering, Politecnico di Milano, Milano, Italy
[b] Quantum Metrology and Nanotechnology division, Istituto Nazionale di Ricerca Metrologica (INRiM), Torino, Italy
[c] Department of Electronics, Information, and Bioengineering, Politecnico di Milano, Milan, Italy

ARTICLE INFO

Keywords:
Structural health monitoring
Fiber optics
Laser interferometry
Strain sensing
Local response function
Surrogate modeling

ABSTRACT

Data routinely collected from distributed fiber-optic cables embedded in civil structures can be repurposed as measurements for structural health monitoring (SHM). However, effectiveness depends critically on fiber-structure coupling and on the ability to infer meaningful structural parameters from the recorded signals. This proof-of-concept study proposes a framework to transform fiber-optic signals, acquired by a recently developed coherent Laser Interferometry (LI) technique, into distributed structural stress fields by combining a calibrated digital twin with surrogate modeling. A finite-element (FE) model is first calibrated using fiber-derived natural frequencies and fiber-averaged strain histories under different fiber-structure coupling conditions, providing a physics-based reference for subsequent strain-to-stress inference. Based on the calibrated FE response, surrogate models are identified via a local response function approach to map fiber-averaged strain to the stress distribution along the beam. Numerical damage scenarios show sensitivity to localized stiffness loss, with the surrogate model reconstructing damage-induced stress redistributions and phase shifts from the fiber signal alone. The proposed framework highlights the potential of repurposing existing communication fiber networks to recover distributed strain and stress fields over large-scale structures when combined with appropriate digital surrogate modeling.

1. Introduction

Monitoring the dynamic response of civil infrastructure through vibration response is a well-established route in modern structural health monitoring (SHM) to infer stiffness changes and track degradation using modal parameters (natural frequencies, damping ratios, and mode shapes) [1–3]. High-sensitivity accelerometer networks for ambient vibration monitoring enable precise modal identification, long-term tracking, and early-stage damage detection [4,5]. In practice, however, high-density monitoring networks remain difficult to scale: installing, powering, and maintaining large networks of conventional sensors can be costly and logistically intrusive, especially in existing buildings. A key point is scalability at the level of infrastructure. Even where fiber-optic (FO) sensors are adopted instead of accelerometers, they are usually installed on a structure-by-structure basis and tailored to each asset. At the same time, urban environments are already traversed by FO telecommunication cables for internet services [6], as illustrated in Fig. 1a. If these fibers can be used as sensing backbones, they could enable wider spatial coverage with minimal additional hardware and disruption.

Optical fiber sensing (OFS) has emerged as a promising candidate for SHM and motivated a broad range of civil engineering applications, including the monitoring of bridges, tunnels, dams, pavements, and tall buildings [7–14]. Comprehensive reviews [15–17] describe the main sensing principles and classify OFS technologies into three primary families: (*i*) point sensors, such as fiber Bragg gratings (FBGs); (*ii*) distributed fiber optic sensors (DFOS), and (*iii*) interferometric systems, which detect nanometric or sub-nanometric deformations by measuring

---

Abbreviations: CNN, Convolutional Neural Network; DAS, distributed acoustic sensing; DFOS, distributed fiber optic sensors; FBG, fiber Bragg grating; FO, fiber-optic; FTTH, fiber-to-the-home; HP, hammer point (impact point); LI, laser interferometry; LRF, local response function; OFS, optical fiber sensing; PCB, piezoelectric accelerometer; PINN, Physics-Informed Neural Network; PSD, power spectral density; SHM, structural health monitoring; TCN, Temporal Convolutional Neural Network.

☆ This article is part of a special issue entitled: 'CAS_ARTISTE25' published in Computers and Structures.

* Corresponding author.
E-mail address: alper.kanyilmaz@polimi.it (A. Kanyilmaz).

https://doi.org/10.1016/j.compstruc.2026.108251
Received 20 December 2025; Accepted 22 April 2026
Available online 11 May 2026
0045-7949/© 2026 The Author(s). Published by Elsevier Ltd. This is an open access article under the CC BY license (http://creativecommons.org/licenses/by/4.0/).

phase differences along distinct optical paths.

Within this landscape, distributed acoustic sensing (DAS) [18–20] and FBG systems [21–23] have developed particularly rapidly and offer dense spatial sampling along the fiber. This enables dynamic monitoring over tens of kilometers with meter-scale spatial resolution, and has been successfully demonstrated for applications such as traffic and bridge vibration monitoring [24], pipeline leak detection [25], and seismic or microtremor recording using dark fibers [26]. However, for civil structures it can face practical limitations related to strain sensitivity and low-frequency fidelity, depending on deployment and processing choices. DFOS can achieve very high displacement/strain sensitivity over the bandwidth relevant to structural dynamics, while operating remotely on installed fibers [27–30]. These characteristics make DFOS attractive for extracting dynamic information from telecom-grade fibers, provided that coupling effects and model interpretation are handled carefully. These systems can achieve sub-nanostrain resolution with bandwidths extending well beyond the typical frequency range of civil structures (0.1–100 Hz). Their relatively simple optical architecture, compactness, and potential for multiplexing make interferometric systems strong candidates for real-world vibration monitoring [31,32].

A key distinction must be made between purpose-installed fiber sensors (e.g., surface-bonded or embedded sensors designed for strain transfer) and existing telecom fiber deployments. Most prior work either uses dedicated fibers under controlled bonding conditions or treats telecom cables as generic sensors without explicitly addressing the uncertain mechanical coupling that governs measurement fidelity in realistic installations. In Fiber-To-The-Home (FTTH) deployments, where fibers are loosely routed, housed in conduits, or otherwise separated from the structural surface, the coupling between the host structure and the optical core is often spatially variable, nonlinear, and poorly characterized, introducing uncertainty in how structural motion appears in the optical signal. This imperfect coupling effectively acts as a mechanical filter, attenuating amplitudes and introducing phase lags that can bias modal estimates. Shear-lag and multilayer models [33–35] show that strain transfer depends strongly on coating and adhesive properties, bonding length, and strain wavelength, while distributed systems are further complicated by spatial variability in coupling stiffness, which can measurably affect apparent damping and modal amplitudes [34–36].

Once reliable FO measurements are available, a central challenge is to reconstruct engineering quantities of interest (stresses, strains, and damage indicators) from sparse or distributed sensor data in (near) real time. Surrogate modelling offers an effective route to this goal, enhancing the scalability of SHM by replacing computationally expensive high-fidelity simulations with fast predictors. Recent contributions have shown how reduced-order and hybrid physics–data approaches can be exploited in this context: Torzoni et al. [37] proposed a non-intrusive framework that combines model order reduction with deep neural networks for real-time simulation under different damage scenarios; Rosafalco et al. [38] used parametric model order reduction and fully convolutional networks for online damage localization; Torzoni et al. [39] extended these ideas to account explicitly for temperature effects in damage classification; and Menghini et al. [40–42] introduced Local Response Function (LRF) surrogates and hybrid virtual-sensing strategies to reconstruct stress histories and stress ranges at non-instrumented locations. Unlocking the potential of telecommunication infrastructure for structural monitoring thus requires a staged validation strategy. Before field deployment on operational structures with active data traffic and unknown coupling conditions, the relationships between fiber attachment configuration, coupling stiffness, and measurement accuracy must be systematically characterized under laboratory conditions, where boundary conditions, material properties, and excitation can be precisely specified. Such controlled investigations provide the physical insight needed to interpret complex fiber signals from real buildings and infrastructure, as well as the basis for robust data processing and modeling frameworks.

In this study, a coherent Laser Interferometry (LI) technique, previously applied to underground deployed telecom fibers for seismicity detection [43], is used for structural vibration monitoring. The interferometer provides a demodulated optical phase time history, which can be converted into an equivalent axial strain response integrated along the fiber path. This measurement reflects deformation accumulated over the routed cable trajectory and depends on how the cable is mechanically coupled to the host structure. In existing telecom deployments, the optical fiber is embedded within non-structural infrastructure (jackets, ducts, fixations, service loops, and local discontinuities), and the measured signal may include amplitude filtering and phase lag that are not purely structural. This limitation reduces the current technology readiness level (TRL) of any “dual-use telecom fiber” SHM concept and motivates conservative claims and staged validation.

In this context, prior controlled laboratory experiments were performed to quantify how FO cable and conduit attachment strategies affect LI-based measurements [44–46]. In the experimental campaign of [46], a simply supported timber beam was instrumented with a dark fiber and accelerometers, and impact tests showed that the interferometric FO system reproduces modal frequencies and strain responses in close agreement with the accelerometers across the investigated coupling configurations, including cases of strong and weak coupling [44–46]. Building on these results, the present study extends the investigation to different coupling configurations to characterise the sensitivity of the proposed strain-to-stress framework to the degree of mechanical coupling between the fiber and the host structure. To this end, a finite element (FE) model of the timber beam is constructed and compared against the experimental acceleration and strain data, and then used to construct a local-response-function surrogate model [40] that maps interferometric FO signals to structural stress fields, enabling extraction of engineering-relevant quantities from fiber-averaged strain measurements.

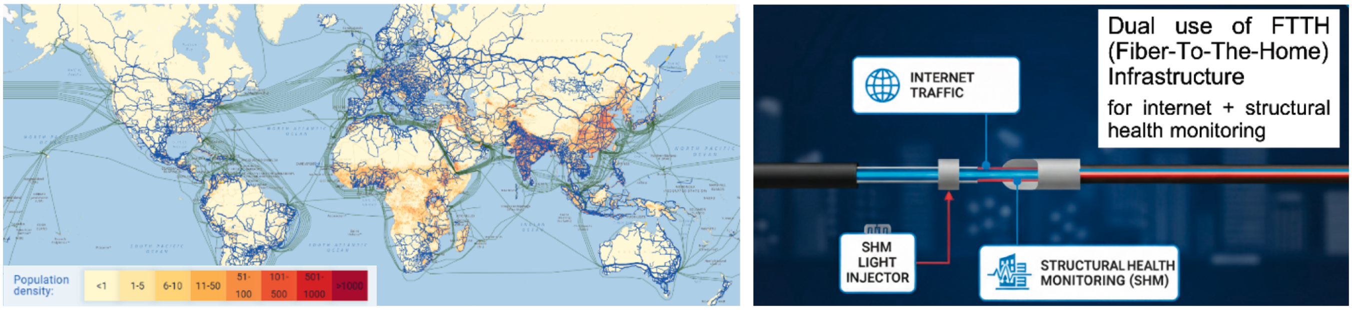

(a) (b)

Fig. 1. (a) Global FO network (≈3,885,787 km) overlaid with population density [6] and (b) a schematic of dual use of FTTH infrastructure for both internet traffic and structural health monitoring.

Despite uncertainties in material properties and boundary conditions, the numerical model reproduces the measured natural frequencies of the first three bending modes and the longitudinal average strain recorded by the dark fiber with discrepancies below 7%. Within this numerical framework, the surrogate model enables the efficient conversion of FO signal data into engineering quantities of interest, such as stresses and vertical/horizontal strain components. A key advantage of the proposed framework is its capability to detect and quantify structural damage through changes in stress distributions and dynamic response patterns. To demonstrate this damage sensitivity, a numerical damage scenario was implemented on the numerical beam model, simulating localized stiffness degradation such as timber deterioration due to moisture ingress or crack formation.

Beyond validating the proposed surrogate-model-based methods under controlled conditions, the findings provide quantitative evidence that FO infrastructure (when appropriately coupled to structures) can be exploited to derive parameters that are critical for structural assessment.

2. Methodology

While the present study focuses on a single fiber path in a controlled laboratory setting, the methodology is intended to scale to multi-channel implementations using multiple branches of existing in-building telecom fibers used for internet connectivity. This configuration is typical of FTTH networks where optical cables route through multiple floors and sections to deliver internet services to individual apartments or offices. LI can remotely detect sub-micrometric changes in the length of deployed FO cables, achieving a resolution lower than 1 μm [43]. Fig. 2 provides the motivation and sensing context for this dual-use concept of existing telecom fibers embedded in the built environment, which are employed as distributed strain sensing paths. The measured fiber response is then linked to a refined FE model for structural interpretations. In earlier work from this study [44–46], an LI–based measurement scheme was presented in which the sensing laser is divided into a reference arm and a measurement arm. The measurement beam is injected into the FO cable and multiplexed with standard data traffic (Fig. 1b). By processing the resulting interference signals, phase variations of the propagating light are recovered and converted into strain integrated along the fiber path [43–46].

The acquisition unit is local and allows data transmission, storage, and processing, enabling continuous strain monitoring of the hosting structure. The recorded strain time histories are subsequently analysed to extract multiple complementary indicators of structural condition. These include global dynamic properties derived from the response (e.g., natural frequencies and damping ratios) as well as local response measures, such as the fiber-averaged strain and the reconstructed stress fields at structural details of interest. The work presented here develops a surrogate-based numerical modelling strategy for exploiting LI measurements in SHM. The existing experimental campaign on the simply supported timber beam is used as a testbed: integrated strain responses are derived from experimentally and numerically computed deformation fields to examine the capability of interferometric measurements to capture structurally relevant information across multiple coupling configurations, as detailed in the flowchart in Fig. 3. The measured FO phase signals are converted into strain time series and combined with numerically obtained local response functions, enabling surrogate predictions of structural stresses at locations not directly monitored.

Local-response-function-based surrogate models can be embedded within a multiscale framework that links a global FE model to locally refined submodels through the displacement field. In this setting, the global FE model is calibrated at the structural scale by comparison with fiber-derived modal parameters (in particular, natural frequencies and, when reliably identifiable, damping ratios). The corresponding nodal displacements (translations and rotations) are then extracted and imposed at the master nodes of the refined substructures to recover local structural parameters of interest for assessment. By coupling interferometric measurements with FE simulations, the proposed framework provides a practical basis for scalable, reliable, and cost-efficient damage assessment in civil structures.

3. Experimental campaign

The experimental campaign was conducted on a simply supported timber beam designed to serve as a reference test structure for the investigations. A detailed description of the experimental campaigns can be found in Ceylan et al. [46]. The test specimen consisted of a softwood beam with a rectangular cross-section of 100 mm × 25 mm and a total length of 3 m. The beam was supported at both ends using a hinge and cylindrical steel rollers with a clear span length of 2.87 m in order to approximate ideal simply supported boundary conditions while minimizing rotational restraint (Fig. 4).

Fig. 5 summarizes sensor locations and hammer impact points on the timber beam. Three PCB accelerometers have been distributed asymmetrically at 0.63, 1.30 and 2.30 m from the left support to maximize observability of the first three bending modes while avoiding nodal positions. For all tests, the FO cable and accelerometers were installed along the top surface of the beam to maintain a consistent curvature-to-strain sign convention. Excitation was applied with an instrumented impact hammer fitted with a soft tip. Five impact points were defined along the span (Fig. 5). At each point, 10 impacts were delivered at ~ 15 s intervals to support repeatability and coefficient-of-variation (c.o.v.) estimates.

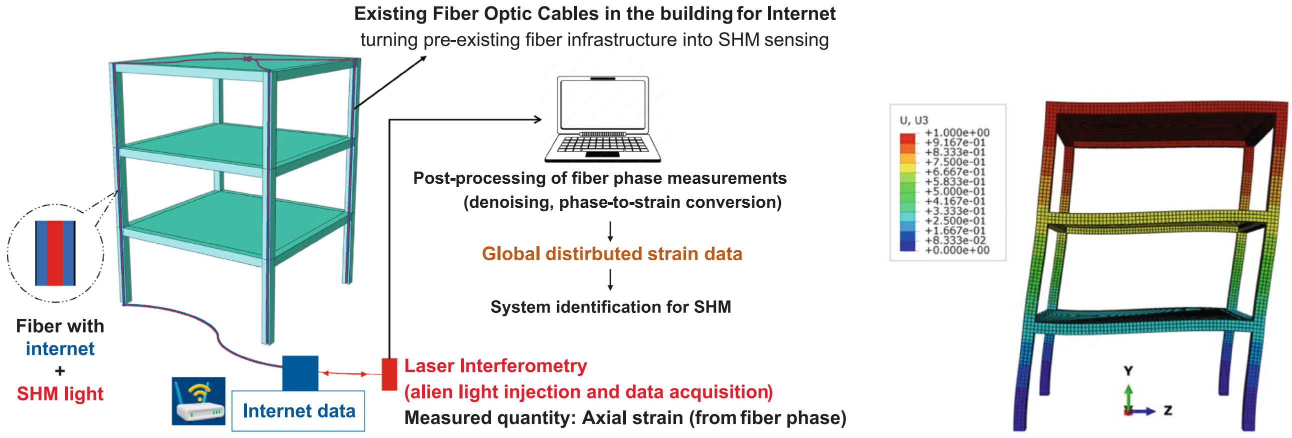

Fig. 2. Motivation and sensing context (dual use of existing telecom fibers as distributed strain sensor) with a representative building linked to a refined FE numerical model.

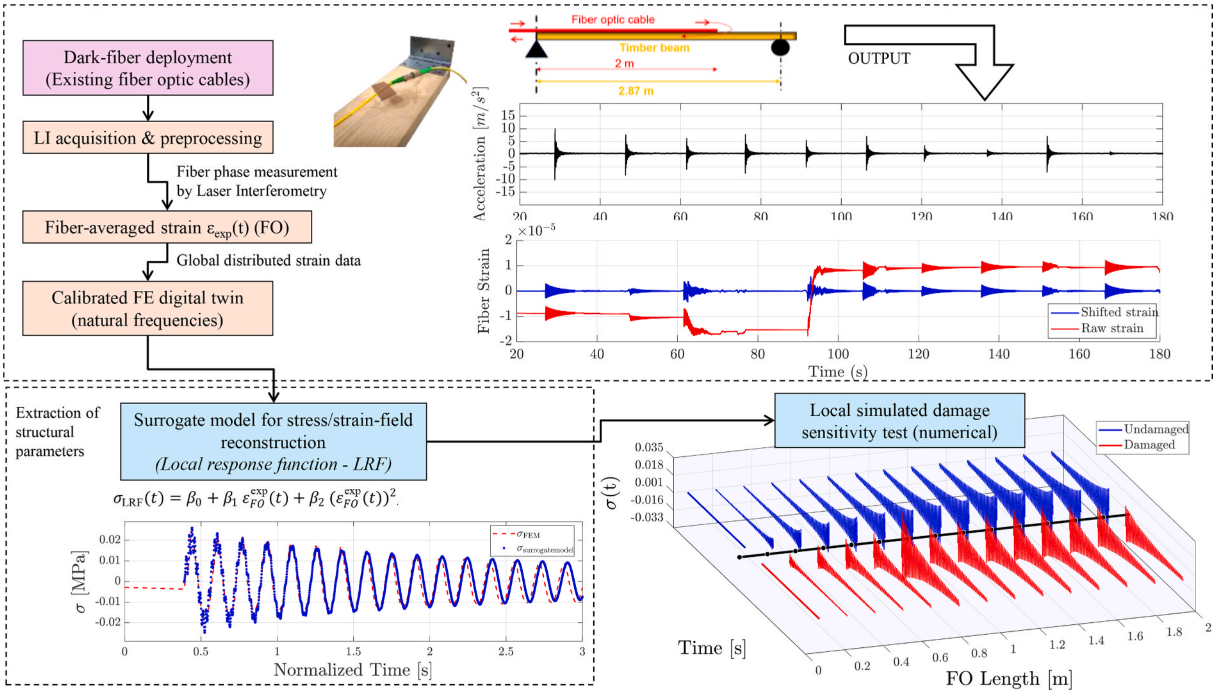

Fig. 3. Methodology flowchart.

Fig. 4. Laboratory setup of the simply supported timber beam test specimen.

The present study considers two reference configurations representing different fiber–structure coupling conditions, which are used consistently in all subsequent analyses. In Configuration 1, the FO cable is taped directly onto the timber beam using strips spaced at approximately 10 cm along the length. In addition, the head connectors at the left and right fiber ends are fixed to the beam with wax, as shown in Fig. 6. This setup provides a controlled and repeatable coupling condition for assessing the performance of the interferometric fiber-optic measurements. In Configuration 2, the FO cable is laid freely on the timber beam without any tape bonding; it is secured only at the pin-supported end to prevent it from slipping or falling off the specimen. The head connectors are also left free in this setup, as shown in Fig. 7. Configuration 2 is used only for comparison purposes to show the strain transfer performance for the free fiber layout.

Fig. 8 summarizes the complete measurement chain used in the laboratory tests, from the optical interferometer to the timber beam. A narrow-linewidth laser source feeds the interferometric device (produced in-house for the purpose of research) in which the optical power is split into a reference arm (internal to the interferometer) and a sensing arm consisting of the deployed dark-fiber segment attached to (and routed through) the timber beam. At the end of the sensing arm, light is reflected back and travels the fiber in the backward direction. It is finally recombined to the reference arm and the resulting interference signal is detected by a photodiode. The photodetector output is digitized using a DAQ/PC acquisition system. The primary measurement provided by the LI setup is a time history of optical phase variation $\Delta\phi(t)$, which reflects strain-induced changes of the optical path length integrated along the sensing fiber. $\Delta\phi(t)$ is demodulated/unwrapped and converted to an equivalent fiber-averaged axial strain history $\varepsilon(t)$, which is the quantity used in the strain-to-stress reconstruction framework. $\varepsilon(t)$ is obtained as follows:

$$\varepsilon(t) = \frac{\Delta\phi(t)}{2\pi}\,\frac{\lambda}{2n_0}\,\frac{1}{L_0(1-p_0)} \tag{1}$$

where $\Delta\phi(t)$ denotes the phase variation (in radians) induced by deformation of the optical fiber, and L_0 is the fiber's undeformed length (2 m in this study). The parameter λ is the laser wavelength, set to 1.542 μm. The refractive index of n_0 is taken as 1.468, while p_0 represents the strain-optic coefficient, assumed to be 0.2 [47].

Fig. 9 and Fig. 10 present the time histories of the hammer-impact

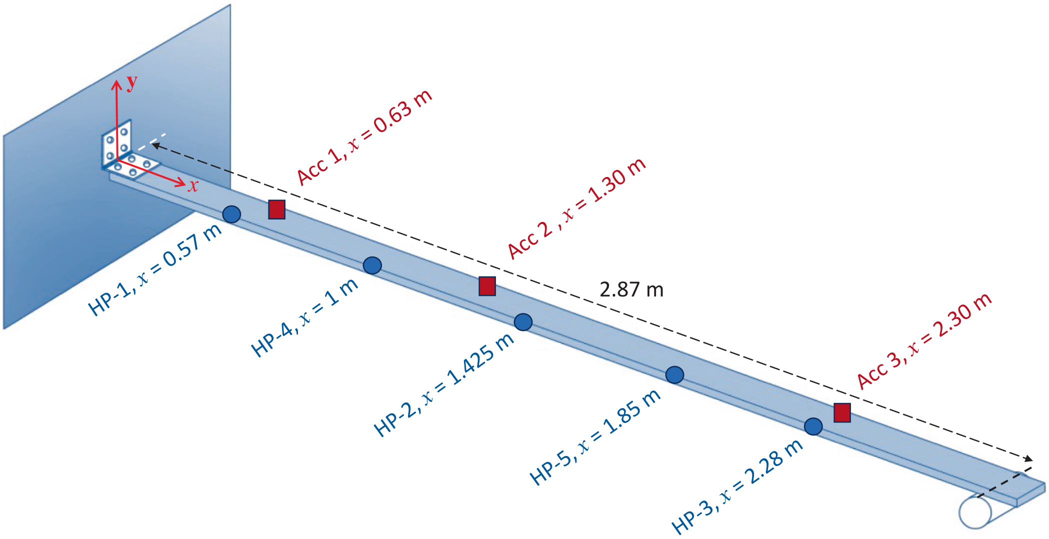

Fig. 5. Configuration of accelerometer positions and hammer impact points along the beam.

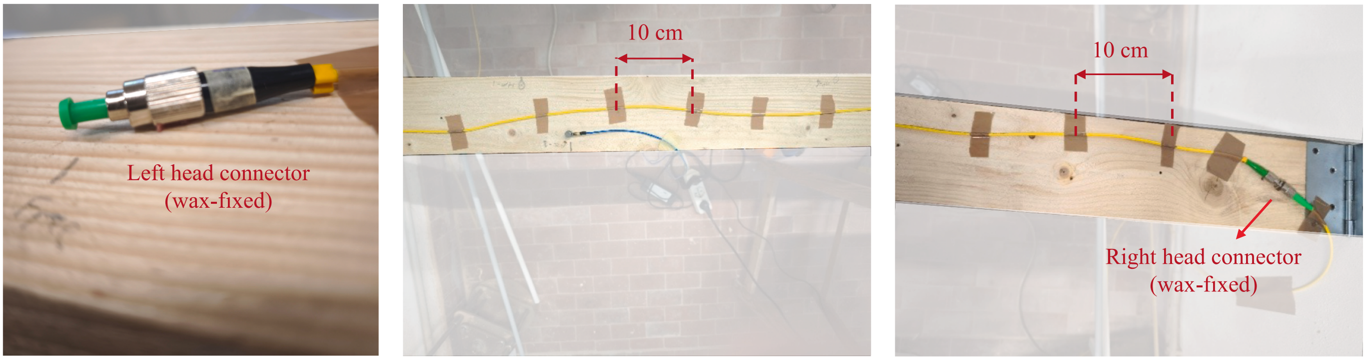

Fig. 6. Configuration 1: Layout of the fiber-optic cable bonded to the bare beam with 10 cm tape spacing.

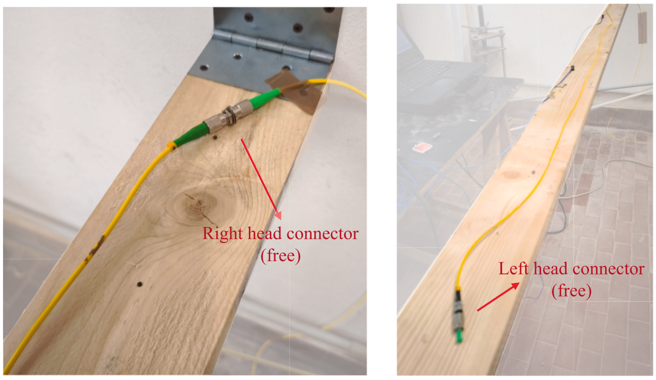

Fig. 7. Configuration 2: Layout of the fiber-optic cable without tape bonding, just taped at the pin supported end.

tests for the impact points HP-2 and HP-4, respectively, for Configuration 1 (coupled, fiber taped). Fig. 9a and Fig. 10a show the input forces measured by the instrumented hammer, with 10 clearly separated impulses of comparable amplitude applied at intervals of roughly 15 s. Fig. 9b and Fig. 10b report the corresponding acceleration responses recorded by the accelerometer Acc-2, which exhibit repeatable transient peaks of about ± 10 m/s^2 and ± 5 m/s^2 following each impact, respectively, indicating stable and essentially linear dynamic behaviour during the impact sequence. Fig. 9c and Fig. 10c present the interferometric FO time histories in terms of axial strain: the red curve shows the raw demodulated strain signal, while the blue curve shows the processed (shifted) strain used in the subsequent analyses in this paper. The raw trace generally displays a slowly varying offset; however, in Fig. 9c a step-like jump appears in the mean level at around $t \approx 90$ s, consistent with a change in the interferometer operating point (e.g., abrupt movement of head connectors or strain relaxation of the fiber cable due to loosening of some bonded tapes) that modifies the quasi-static reference strain without affecting the dynamic component. To obtain a physically consistent strain history, the raw strain signals were therefore recentered by removing the segment-wise mean and correcting for the offset, yielding the shifted strain in blue, whose transient content aligns with the hammer impacts and the accelerometer responses. A slow-varying offset is estimated using moving-median smoothing and change-point segmentation and subtracted from the signal. Finally, a high-pass Butterworth filter (0.5 Hz) removes residual quasi-static components, centering the strain around zero and retaining only the dynamic response. The strain measured during the test on HP-2 varies between approximately -1.78×10^{-5} and $+ 1.22 \times 10^{-5}$, with an average amplitude of $\Delta\varepsilon \approx 4.99 \cdot 10^{-6} \approx 5$ με. Further, the strain measured during the test on HP-4 varies between approximately -6.27×10^{-6} and $+ 4.51 \times 10^{-6}$, with an average amplitude of $\Delta\varepsilon \approx 1.76 \times 10^{-6} \approx 1.8$ με.

The interferometer outputs a demodulated phase time history, which is converted into the fiber-averaged axial strain $\varepsilon(t)$ by using Eq. (1).

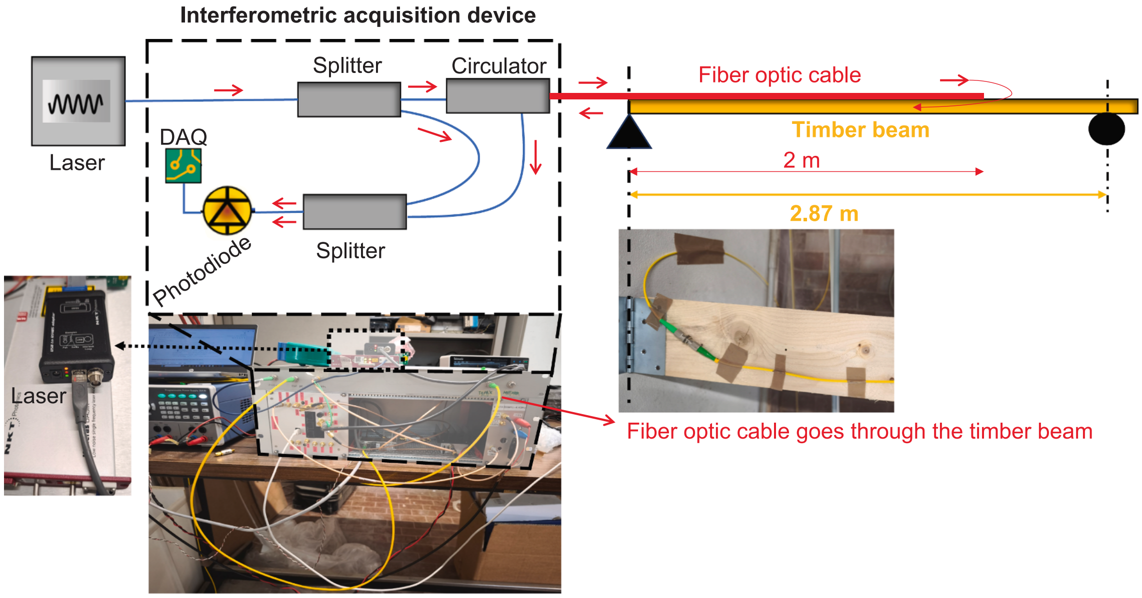

Fig. 8. Full experimental and acquisition setup for interferometric dark-fiber measurements on the timber beam. Top Left: schematic of the interferometric acquisition device (laser source, splitter, circulator, photodiode, and DAQ) and signal flow. Top Right: sensing fiber routed through the timber beam (deployed fiber length is 2 m; beam clear span 2.87 m). Bottom: photographs of the laser source, interferometric acquisition device and the fiber entering to the timber beam.

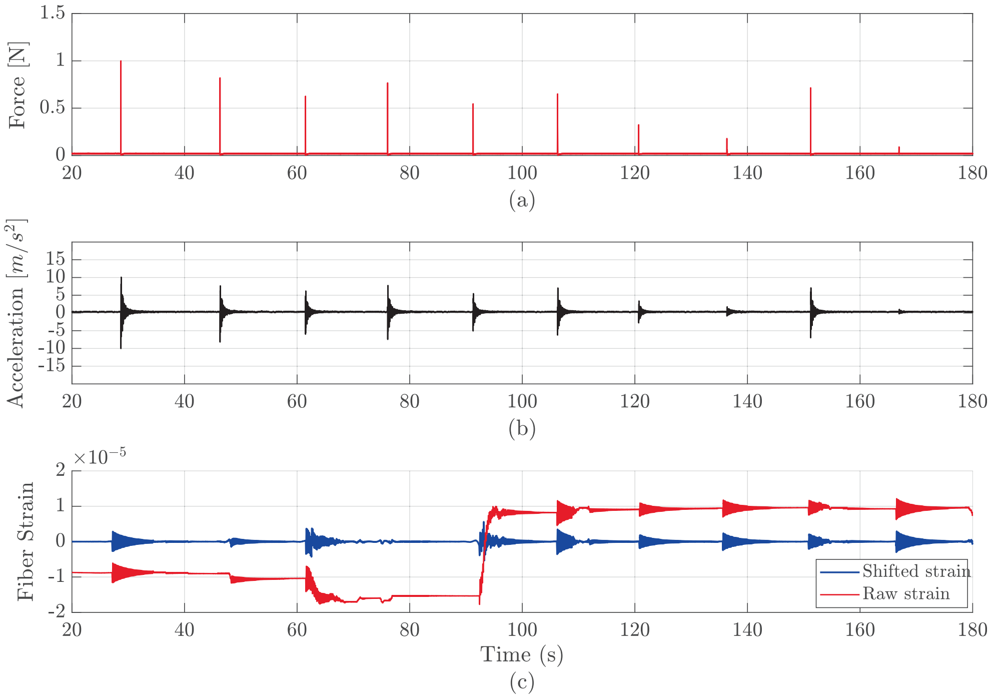

Fig. 9. Configuration 1: (a) Hammer impact loadings at the impact point of HP-2, (b) acceleration time history measured by the accelerometer Acc2, and (c) axial fiber strain time history for a time period of 20–180 s (red line: raw strain response, blue line: processed strain response).

Fig. 11 shows the power spectral density (PSD) of the FO phase signal, for hammer impact points HP-2 and HP-4, corresponding to the raw strain traces provided in Fig. 9c and Fig. 10c, respectively. The PSDs are computed from the entire recorded time history for each impact-point test. The PSD of the FO phase is estimated using Welch's method after resampling to 200 Hz. As an example for HP-2, the original record consists of 160,000 samples at 1000 Hz (160 s), corresponding to 32,000 samples after resampling. Welch's method uses a Hann window of 3,200 samples with 50% overlap and number of FFT points 3,200, resulting in a frequency resolution $\Delta f = 200\ \text{Hz}/3200 \approx 0.0625\ \text{Hz}$ and 19 averaged segments. All the PSDs are computed with the same approach in this study. Modal frequencies are identified for each hammer test via peak picking of the dominant PSD peaks. Table 1 shows the first three modal frequencies and damping ratios obtained from FO phase data at each hammer test in Configuration 1, with the average and c.o.v. The average values are compared with those identified from the accelerometer data in Table 2. Results show very good agreement between the identified modal frequencies.

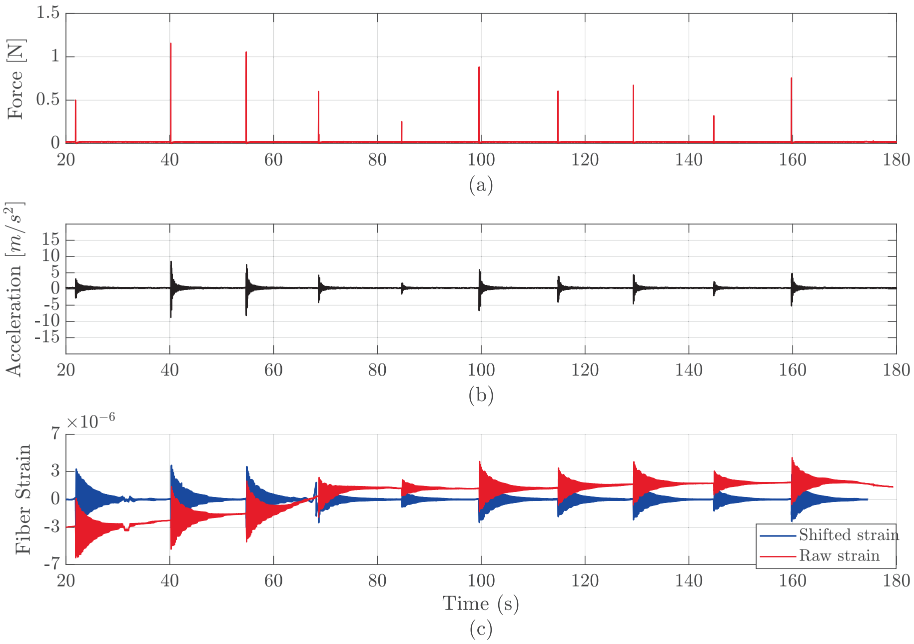

Fig. 10. Configuration 1: (a) Hammer impact loadings at the impact point of HP-4, (b) acceleration time history measured by the accelerometer Acc2, and (c) axial fiber strain time history for a time period of 20–180 s (red line: raw strain response, blue line: processed strain response).

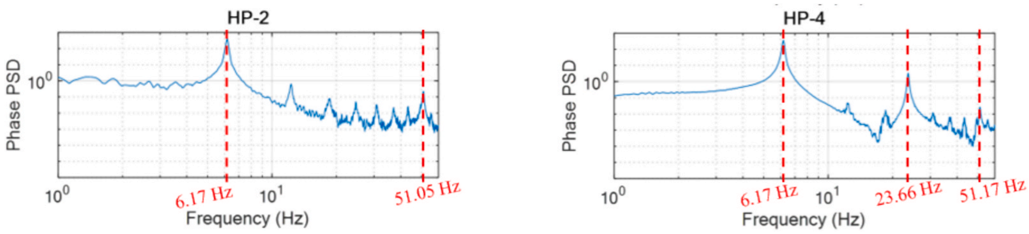

Fig. 11. Power spectral density of the FO cable phase signal for HP-2 and HP-4 hammer impact points [44].

Table 1

First 3 modal frequencies f (Hz) and modal damping ratios ζ (%) obtained from FO phase at each hammer test.

Impact Point	Mode 1		Mode 2		Mode 3	
	f_1	ζ_1	f_2	ζ_2	f_3	ζ_3
HP-2	6.17	0.71	–	–	51.05	0.50
HP-4	6.17	0.72	23.66	0.46	51.17	0.43
Mean (all HP points)	6.17	0.78	23.65	0.48	51.08	0.43
c.o.v (%)	0.09	9.90	0.02	2.68	0.13	11.29

Table 2

Comparison of modal frequencies (Hz) identified from acceleration and FO phase data.

	Accelerometers	FO phase data (LI)	Relative Difference (%)
Mode 1	6.17	6.17	0
Mode 2	23.65	23.65	0
Mode 3	51.08	51.08	0

4. Numerical modelling for prediction of structural parameters

A numerical beam model was developed in MIDAS Gen [48] to provide a digital representation of the experimental setup and to support stress-field reconstruction from fibre-path–averaged strain measurements. The model serves two purposes: (*i*) reproducing the measured dynamic response of the simply supported timber beam, and (*ii*) generating consistent input–output datasets for calibrating a local response function (LRF) surrogate that maps interferometric fibre strain to local structural stress histories. Accordingly, the experiments/FE comparison is introduced as a validation step to establish a digital twin suitable for subsequent strain-to-stress surrogate identification.

4.1. Finite element model of the timber beam

The numerical model reproduces the geometry, boundary conditions, and loading configuration described in Section 3. Linear elastic, homogeneous, and isotropic behaviour is assumed for the timber. The density is taken as $\rho = 500$ kg/m^3, while the Young's modulus $E = 10\,GPa$. The beam is discretised using one-dimensional Euler–Bernoulli beam elements with uniform cross-section along the span. The mesh density is chosen such that the element length is sufficiently small to accommodate the bending wavelength associated with the third mode, ensuring an accurate representation of the first three bending modes. The supports are modelled as an ideal pin at one end and a roller at the other, reproducing the hinge–roller configuration used in the laboratory and approximating simply supported boundary conditions with minimal rotational restraint. Time-history analyses were performed using the implicit Newmark-β scheme ($\beta = 1/4$, $\gamma = 1/2$) with a constant time step $\Delta t = 0.001$ s. This choice ensured numerical stability and adequate resolution of the dynamic response up to 500 Hz.

Damping is included to reproduce the experimentally observed decay rate of the transient response and to support a consistent time-history-based strain-to-stress mapping. The first three bending-mode damping ratios identified from the FO phase data (Table 1) are adopted (mean values): $\zeta_1 = 0.78\%$, $\zeta_2 = 0.48\%$, $\zeta_3 = 0.43\%$. These ratios are implemented as classical viscous (modal) damping: an equivalent damping matrix is constructed in physical coordinates so that the selected modes exhibit the assigned ζ_i, and the resulting system is then integrated in time using the Newmark scheme in the nodal (physical) basis.

To simulate the impact tests, the hammer excitation at a given hammer point (e.g. HP-2) is represented as a vertical concentrated load applied at the corresponding node of the beam model. A load of 1 N, consistent with the measured input force, is applied using a triangular time history with a total duration of 0.02 s, reaching its peak value at $t = 0.01$ s. An eigenvalue analysis of the calibrated model yields the first three bending modes with natural frequencies $f_1 = 6.09$ Hz, $f_2 = 24.37$ Hz, and $f_3 = 54.06$ Hz (Fig. 12). These values are in good agreement with the mean frequencies identified from FO phase data, $f_1^{\exp} = 6.17$ Hz, $f_2^{\exp} = 23.65$ Hz and $f_3^{\exp} = 51.08$ Hz (Table 1), with relative discrepancies of approximately -1.3%, $+3.0\%$ and $+5.9\%$, respectively. The corresponding numerical mode shapes, shown in Fig. 12, closely resemble the experimental shapes obtained from accelerometer measurements as discussed in [46].

Fig. 13a–c compares the measured acceleration from the installed accelerometer Acc2 due to HP-2 (Fig. 13-a), and the strain obtained from the FO signal data of Configuration 1 (taped fiber, coupled) with the corresponding responses predicted by the FE model due to HP-2 and HP-4 (Fig. 13-b–c), showing good overall agreement. The error in terms of maximum peak strain is approximately 7%. Fig. 14 compares the FE results and experimental measurements from Configuration 2 (free fiber, uncoupled) in terms of strain due to HP-2. Fig. 15-a (HP-2) and Fig. 15-b (HP-4) report the PSD of the strain time history provided in Fig. 13-b-c and Fig. 14, where the first and third natural modes of the structure are clearly identified. The largest discrepancy is observed for the third mode, with an experimental frequency of 51.08 Hz compared to 54.06 Hz predicted by the FE model; however, this difference remains below a maximum error of 6%. This threshold is considered acceptable in light of typical uncertainties in material properties, boundary conditions, and measurement precision. The maximum modal frequency errors obtained for the second configuration (free fiber, uncoupled) are 3.1%, 5.0%, and 7.4% for the first, second, and third bending modes, respectively compared to taped configuration. The progressive increase in discrepancy with mode order is consistent with the reduced coupling stiffness in this configuration: the absence of tape bonding allows minor local fiber displacements, which attenuate high-frequency strain components more severely than low-frequency ones, leading to a gradual degradation of agreement with the FE predictions relative to the taped configuration. It is worth noting that, in a general continuous monitoring scenario where PSDs are estimated from strain time histories spanning multiple excitation events, the frequency error associated with a free-fiber deployment is partly stochastic (varying with the instantaneous contact condition at each event) and would therefore be progressively reduced by averaging modal frequencies across successive events, improving agreement with a fully coupled configuration.

In this laboratory benchmark, material properties are assigned as fixed values (e.g., $\rho = 500$ kg/m^3, while $E = 10\,GPa$) to reflect the controlled specimen and to isolate the performance of the proposed strain-to-stress reconstruction workflow. At structural scale for field applications, material parameters and boundary-condition stiffness are generally uncertain and should therefore be introduced as bounded variables informed by engineering priors (design documentation, code-based ranges, and/or limited in-situ information). In that case, the global FE model can be calibrated probabilistically against measured dynamic features (e.g., modal frequencies and response characteristics extracted from the FO signal, possibly complemented by auxiliary sensors) using, for example, Bayesian model updating with uncertainty quantification. The resulting parameter uncertainty can then be propagated through the FE–surrogate mapping to report reconstructed stress quantities with uncertainty bounds rather than as single deterministic estimates.

The beam is selected as a low-order simple benchmark to clearly demonstrate the end-to-end workflow, focusing on the frequency band in which the LI-derived response exhibits high fidelity and the modal content is clearly identifiable.

The strain signal derived from Configuration 2 (fiber cable is free) is also plotted against the numerical results in Fig. 14. Although a shift is observed between the peak strain values, the overall signal magnitudes remain in reasonable agreement with the FE predictions, suggesting that the proposed framework retains its applicability to uncoupled or loosely coupled fiber-optic deployments — a particularly relevant finding in the context of existing FTTH infrastructure, where controlled bonding conditions are generally unavailable. For higher-order complex structures with higher-frequency ranges, increased modal density, reduced measurement signal to noise ratio, and coupling-induced filtering can complicate identification and may influence local stress gradients. In such cases, peak picking may be insufficient. Practical implementation would therefore rely on a reliable operational bandwidth and use band-limited, parametric identification methods together with reduced-order modeling to retain the modes that contribute materially to surrogate-based stress reconstruction. A systematic treatment of dense-modal and high-frequency regimes is left for future work.

5. Local response function for stress reconstruction

While the interferometric system directly provides a time history of fibre-averaged axial strain along the dark fibre path, structural assessment often requires local quantities such as bending stresses at specific sections or details. To bridge this gap, a local response function (LRF) approach, proposed by Menghini et al. [40–42], is adopted to relate the fibre-averaged strain to local stresses computed from the FE model. In general, the LRF assumes that the local stress $\sigma(t)$ at time t can be approximated as:

$$\widehat{\sigma}(t_k) = f(x(t_k)) + \xi(t_k), k = 1, \cdots, N, \tag{2}$$

where $x(t)$ is the chosen control variable (vector-valued), $f(\cdot)$ is an unknown response function, and $\xi(t)$ is a residual error term assumed to follow a normal distribution with zero mean. In this work, the optic fiber-averaged strain $\varepsilon_{FO}(t)$ is identified as the control variable, so that $x(t) = \varepsilon_{FO}(t)$. $f(\cdot)$ can be then approximated using a low-order polynomial, i.e., an LRF of the form:

$$\sigma(t_k) \approx f(\varepsilon_{FO}(t_k)) = \beta_0 + \beta_1\, \varepsilon_{FO}(t_k) + \beta_2\, \varepsilon_{FO}^2(t_k) + \cdots + \beta_m\, \varepsilon_{FO}^m(t_k), \tag{3}$$

where β_j are unknown coefficients to be identified. In the present study, we use a quadratic model ($m = 2$), namely

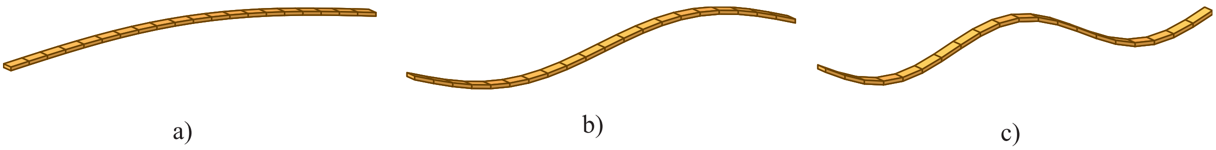
a) b) c)

Fig. 12. Numerical mode shapes. (a) Bending mode 1 ($f_1 = 6.09$ Hz); (b) Bending mode 2 ($f_2 = 24.37$ Hz), (c) Bending mode 3 ($f_3 = 54.06$ Hz); (d) impact load equal to 1.00 N on HP-2 point ($t = 0.25$ s).

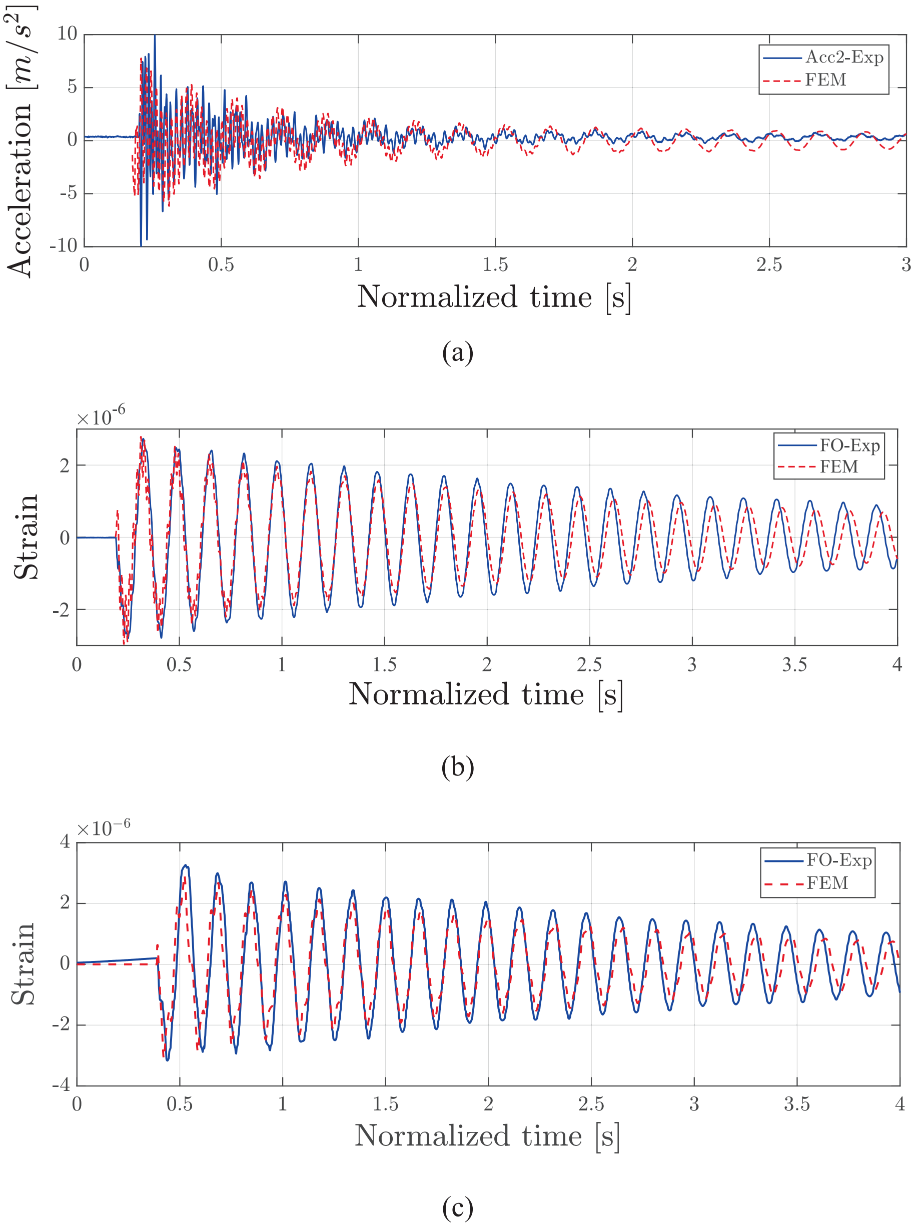

Fig. 13. Configuration 1: Comparison between FE results and experimental measurements with taped coupling: (a) acceleration HP-2; (b) Strain HP-2; (c) Strain HP-4 ringdown segment after a single impact.

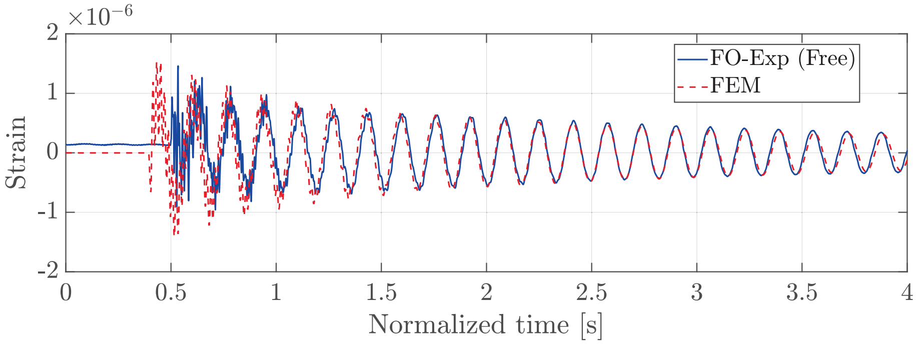

Fig. 14. Configuration 2: Comparison between FE results and experimental measurements without taped coupling (fiber is free on the beam, taped at the pin supported end only) in terms of Strain HP-2 for a single impact.

$$\sigma(t_k) \approx \beta_0 + \beta_1\, \varepsilon_{FO}(t_k) + \beta_2\, \varepsilon^2_{FO}(t_k). \tag{4}$$

The coefficients $\beta = [\beta_0\, \beta_1\, \beta_2]^\top$ are estimated by least squares, using the

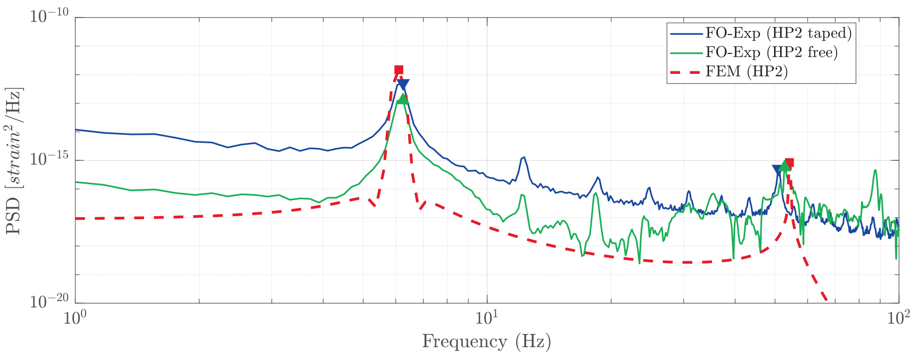

(a)

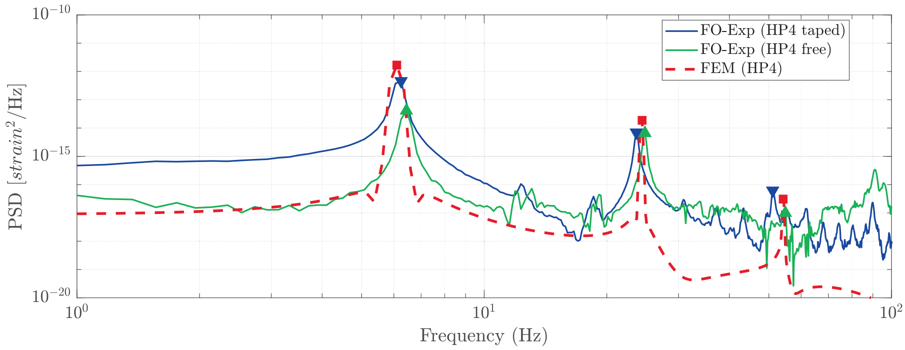

(b)

Fig. 15. Comparison between the PSDs of the FE results and experimental measurements for a) HP-2; b) HP-4 under coupled (Configuration 1, taped fiber) and uncoupled (Configuration 2, free fiber) conditions.

time histories of stress from the local FE model as calibration data and the corresponding numerically computed fiber strain under the same hammer excitation. Defining the vector of FEM stresses:

$$\boldsymbol{\sigma}^{\mathrm{FEM}} = \begin{bmatrix} \sigma^{\mathrm{FEM}}(t_1) \\ \vdots \\ \sigma^{\mathrm{FEM}}(t_N) \end{bmatrix}, \tag{5}$$

and the regression matrix for the quadratic model:

$$\mathbf{X} = \begin{bmatrix} 1 & \varepsilon_{FO}(t_1) & \varepsilon_{FO}^2(t_1) \\ \vdots & \vdots & \vdots \\ 1 & \varepsilon_{FO}(t_N) & \varepsilon_{FO}^2(t_N) \end{bmatrix}, \tag{6}$$

The calibration problem can be written in compact form as:

$$\boldsymbol{\sigma}^{\mathrm{FEM}} = \mathbf{X}\boldsymbol{\beta} + \boldsymbol{\xi}, \tag{7}$$

so that the least-squares estimate is:

$$\boldsymbol{\beta} = (\mathbf{X}^{\top}\mathbf{X})^{-1}\mathbf{X}^{\top}\boldsymbol{\sigma}^{\mathrm{FEM}}. \tag{8}$$

This corresponds to the polynomial fit on a selected time window with high signal-to-noise ratio. The goodness of fit is quantified by the coefficient of determination R^2, the root mean square error (RMSE), and the Pearson correlation coefficient between FEM and reconstructed stress. Once the LRF has been identified, the stress history is reconstructed directly from the experimental fiber strain measurements $\varepsilon_f^{\mathrm{exp}}(t)$ as:

$$\sigma_{\mathrm{LRF}}(t) = \beta_0 + \beta_1\, \varepsilon_{FO}^{\mathrm{exp}}(t) + \beta_2\, \left(\varepsilon_{FO}^{\mathrm{exp}}(t)\right)^2, \tag{9}$$

providing an estimate of the stress in the structural detail of interest from a single FO measurement and the calibrated numerical model. Fig. 16-a-b shows the predicted stress by surrogate models and by FEM showing a good agreement for HP-2 and HP-4, respectively.

Notably, Fig. 16-c illustrates the correlation between numerical stress and the measured average FO strain. This correlation is very high ($\rho > 0.9$) for the first signal, in the time window between 15 s and 25 s. However, the Pearson correlation coefficient is highly sensitive to noise in the data, and when all samples are used to construct the surrogate model, the resulting correlation can decrease, reducing the accuracy of the final results. In particular, when the relationship between variables is very complex, the LRF approach, which assumes a polynomial relation between a response parameter and a control variable, may be insufficient. This limitation becomes more pronounced when the measured FO signal represents a spatially averaged strain over a finite influence length, while the structural response varies over shorter characteristic lengths (e.g., near concentrated loads, supports, or local stiffness changes). In such cases, the strain-to-stress mapping becomes effectively nonlocal and may require explicit treatment of the spatial filtering (e.g., convolution/regularization) or more expressive surrogates. In such cases, it becomes necessary to integrate more expressive models, such as Convolutional or Temporal Neural network (CNN/TCN)-based architectures [42,49] or Physics-Informed Neural Networks (PINNs), to reconstruct the underlying temporal correlations in a more accurate and robust approach [50]. The results of this approach show that structural stresses at unmonitored locations can be predicted from the FO signal by using numerically estimated LRFs. From a practical perspective for real buildings, the FO signals can be converted into structural stresses through a surrogate model of the structure.

More generally, the use of surrogate models to predict stresses and strains can be integrated into a broader multi-scale framework. In such a scheme, the calibrated global FE model is driven by fibre-derived quantities, and its nodal displacements are used as boundary conditions for refined local submodels of structural details. Surrogate models can then be identified between the global response (e.g. fibre strain or

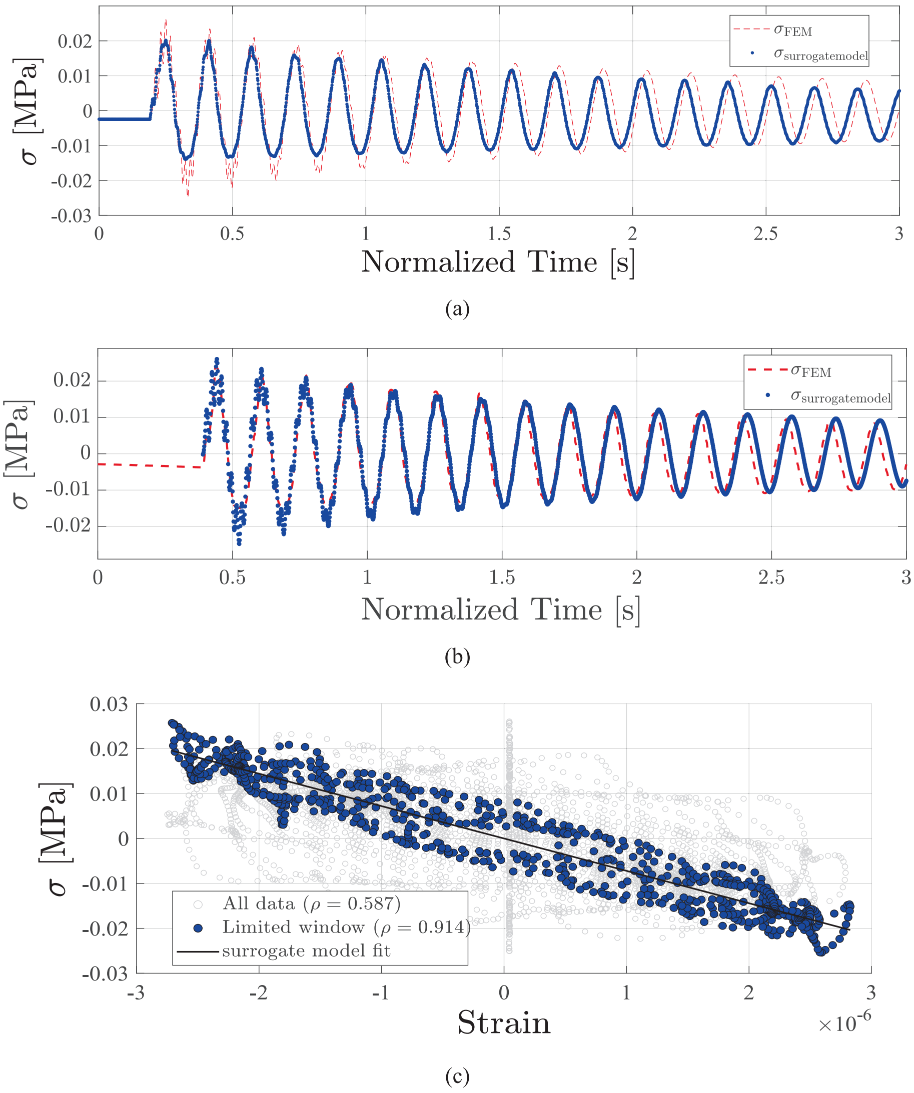

(a)

(b)

(c)

Fig. 16. Comparison between FE results and experimental measurements: (a) bending stress in the upper midspan timber fibre HP-2; (b) bending stress in the upper midspan timber fibre HP-4; (c) time-history correlation between predicted FE stress and measured strain.

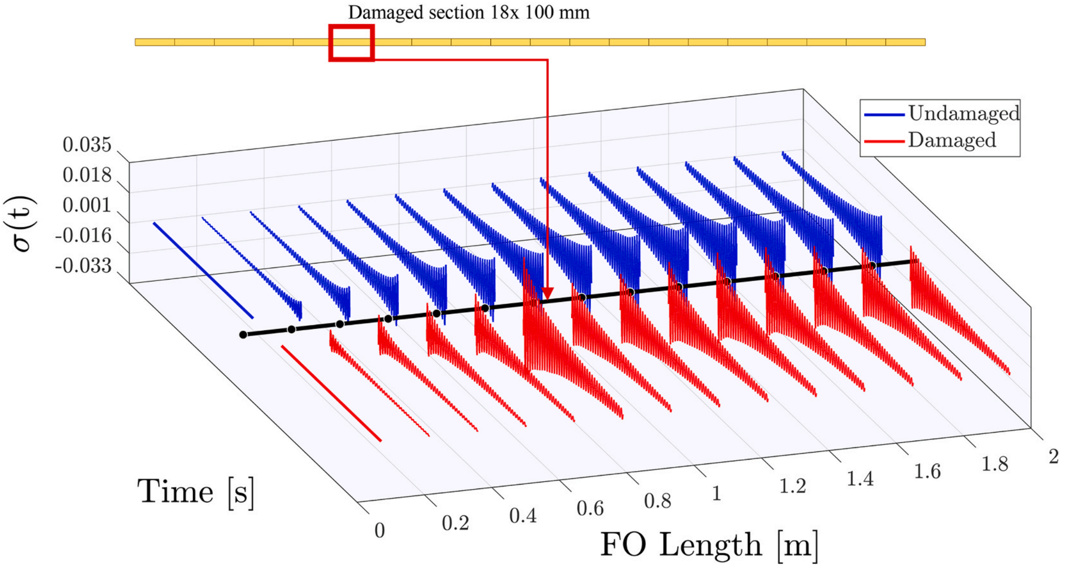

Fig. 17. Predicted stress histories along the dark fiber obtained from surrogate models (HP-2).

nodal displacements) and the internal forces or stresses in these submodels, enabling efficient reconstruction of stress and strain components at locations that are not directly instrumented. This provides a computationally efficient pathway to exploit interferometric fibre measurements for structural assessment of more complex buildings and infrastructure systems. Once the global FE time-history is available, the surrogate coefficients can be identified in batch for multiple sections/details with negligible additional computational cost. In operation, coefficients calibrated for the baseline (undamaged) state provide a reference predictor, and persistent deviations between predicted and measured fibre-derived responses can be used to flag potential stiffness changes and trigger model updating. To evaluate how sensitive the inferred stresses (from dark–FO measurements and surrogate models) are to local damage, the cross–section located 0.86 m from the pin support was intentionally reduced from 25 × 100 mm to 18 × 100 mm over a 0.14 m segment, simulating a localized stiffness loss. The selected 28% section reduction represents a stiffness-loss scenario introduced for proof-of-concept purposes; quantifying detection thresholds for more subtle damage mechanisms is left to future work. This configuration is illustrated globally in Fig. 17, where the blue curves show the stress time

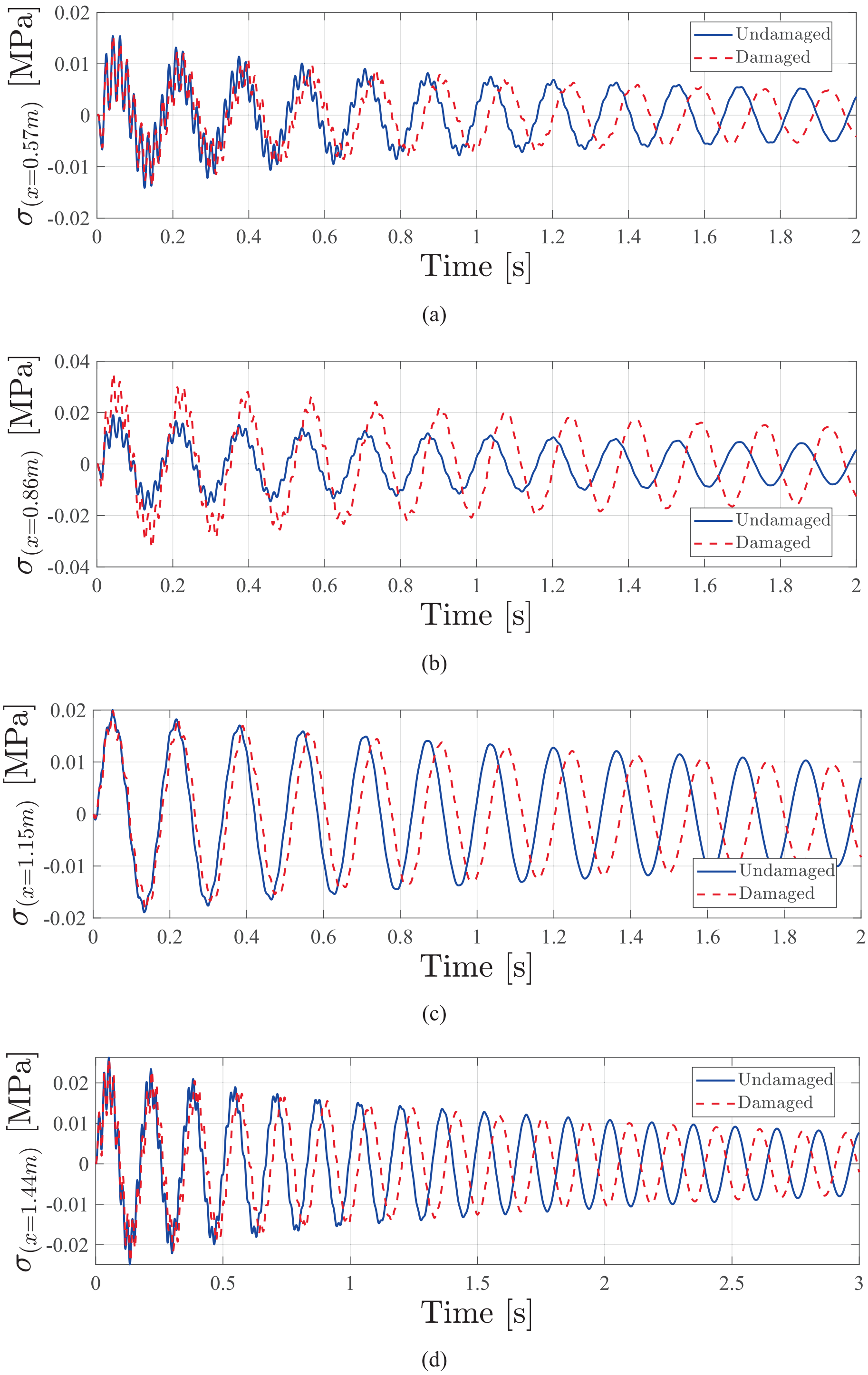

(a)

(b)

(c)

(d)

Fig. 18. Predicted stress histories from surrogate models. (a) x = 0.57 m section; (b) x = 0.86 m section (damaged section); (c) x = 1.15 m section; (d) x = 1.44 m section (midspan section).

histories along the FO cable for all segments into which the cable has been subdivided, and the red curves show the corresponding stress time histories under the damaged condition (reduced resistant section 18 × 100 mm).

Fig. 18 shows the predicted stress time histories at several cross-sections along the beam: (a) $x = 0.57$ m, (b) $x = 0.86$ m (damaged section), (c) $x = 1.15$ m, and (d) $x = 1.44$ m (midspan). Fig. 18-b corresponds to the damaged cross-section. In addition to the marked stress reduction at the damaged section, a frequency shift of the stress histories can be observed at all locations (Fig. 18a-d). These results indicate that the proposed method can be used for structural integrity monitoring and is able to quantify the changes in key mechanical parameters induced by damage. Although demonstrated here on a simply supported timber beam, extension to large-scale applications will require site-specific coupling characterization and coupling uncertainty modeling of the fibers, adapting the method for arbitrary multi-branch FTTH routing, probabilistic model updating on building-scale models that involves uncertainty quantification, robust identification in dense-modal cases of complex structures, and progressive validation on building specimens and field deployments before realistic degradation mechanisms can be interpreted with confidence. The comparison between intact and damaged configurations reveals multiple damage-sensitive features. Indeed, a clear frequency shift of approximately 166 Hz is observed in the stress histories at both the damaged section and midspan (Fig. 18a-d). This frequency indicates altered wave propagation characteristics and modified modal response, which persist even at locations remote from the damage. A key practical implication is that such damage-induced deviations are inherently time-localized: unlike systematic discrepancies arising from modeling imperfections or parameter uncertainty, which remain approximately constant over the monitoring period, damage-related signatures emerge at a specific point in time and persist thereafter, making them distinguishable from stationary baseline errors in the surrogate predictions. Moreover, the peak stress at midspan increased by 89%, suggesting load redistribution from the weakened section, a classic indicator of structural damage that can be captured through the fiber-averaged strain alone.

The surrogate model successfully reconstructs all these damage-induced changes from the FO measurements, demonstrating that the computational framework preserves damage-sensitive information throughout the strain-to-stress transformation. Notably, these indicators emerge without requiring high-density sensor arrays: a single fiber path combined with the calibrated numerical model suffices to identify both the presence and approximate location of damage through the characteristic stress redistribution pattern. The along-fiber representation in Fig. 17 is used for visualization; near structural discontinuities the methodology should be applied piecewise with dedicated local sub-models/surrogates.

6. Conclusion

This work presented a numerical framework for stress-field reconstruction from dark-fiber strain measurements, combining a calibrated finite element (FE) digital twin with a quadratic local response-function (LRF) surrogate. The approach uses fiber-averaged strain as input to infer bending-stress histories at monitored and non-instrumented sections, enabling a distributed interpretation of structural response from sparse fiber instrumentation.

- The calibrated FE model provides an adequate digital twin for inverse stress reconstruction.
- The quadratic LRF surrogate recovers bending-stress time histories at monitored sections and supports extrapolation of stresses (and directional strain components) to locations not directly instrumented, yielding a distributed stress representation along the beam.
- Damage sensitivity was assessed through a 28% cross-sectional reduction, which produced consistent signatures in reconstructed indicators (stress amplitude changes, phase shifts, and load redistribution), detectable also away from the damaged section and therefore compatible with system-level detection under sparse sensing.
- Compared with frequency-only monitoring, the reconstructed stress/strain information provides directly interpretable demand measures (time histories and redistribution patterns) that complement global modal shifts and improve the engineering interpretation of degradation.

The present study is subject to certain limitations that should be mentioned. First, the numerical model has been validated only for the intact structural configuration; its predictive accuracy under damage conditions remains to be experimentally verified. Second, the surrogate performance is inherently tied to the fidelity with which the numerical model captures the structural complexity, which may lead to optimistic accuracy estimates for localized features. Furthermore, the reasonable agreement observed between the numerical predictions and the strain signal from the uncoupled configuration indicates that the method may extend beyond controlled bonding conditions, motivating future systematic investigation of coupling-independent or weakly coupled deployments relevant to real FTTH infrastructure.

Future work should therefore include: (i) experimental testing of damaged configurations to validate model predictions under various degradation scenarios; (ii) experimental and numerical investigation of alternative conduit layouts, including coupled and series arrangements, to assess the method's sensitivity and spatial resolution; and (iii) extension to more complex damage patterns and environmental conditions, in order to establish the robustness of the framework for real-world structural health monitoring (SHM) applications.

More broadly, future developments will aim to extend this approach to full-scale buildings and more complex structural systems, incorporating long-term monitoring under environmental variability as well as fiber networks embedded within existing telecommunication infrastructure. In such full-scale deployments, robust calibration of the global model under uncertain material properties and boundary conditions will be essential, and reconstructed stress fields should be reported with uncertainty bounds obtained by propagating these uncertainties through the FE–surrogate chain.

CRediT authorship contribution statement

Alessandro Menghini: Writing – original draft, Supervision, Software, Project administration, Methodology, Investigation, Formal analysis, Conceptualization. **Hasan Ceylan:** Writing – original draft, Visualization, Validation, Resources, Project administration, Methodology, Investigation, Funding acquisition, Formal analysis, Conceptualization. **Alper Kanyilmaz:** Visualization, Validation, Supervision, Resources, Project administration, Methodology, Investigation, Funding acquisition, Formal analysis, Conceptualization. **Simone Donadello:** Validation, Supervision, Software, Resources, Methodology, Investigation, Funding acquisition, Formal analysis, Data curation. **Cecilia Clivati:** Validation, Supervision, Resources, Investigation, Funding acquisition, Formal analysis, Data curation. **Daniele Loiacono:** Supervision, Software, Project administration, Methodology, Investigation, Formal analysis, Data curation.

Declaration of competing interest

The authors declare that they have no known competing financial interests or personal relationships that could have appeared to influence the work reported in this paper.

Acknowledgements

This study was conducted as part of the FORESIGHT project, which has received funding from the European Union’s Horizon Europe 2023 research and innovation programme under the Marie Skłodowska-Curie Actions (MSCA) Postdoctoral Fellowship (Grant Agreement No. 101153201). The authors gratefully acknowledge this support. Views and opinions expressed are, however, those of the authors only and do not necessarily reflect those of the European Union. Neither the European Union nor the granting authority can be held responsible for them.

References

[1] Doebling SW, Farrar CR, Prime MB, Shevitz DW. Damage identification and health monitoring of structural and mechanical systems from changes in their vibration characteristics: a literature review (LA-13070-MS). Los Alamos National Laboratory 1996. https://doi.org/10.2172/249299.

[2] Farrar CR, Lieven NAJ. Damage prognosis: the future of structural health monitoring. Philos Trans R Soc A Math Phys Eng Sci 2007;365(1851):623–32. https://doi.org/10.1098/rsta.2006.1927.

[3] Castiglioni CA, Drei A, Kanyilmaz A. Continuous monitoring of Service Conditions of a Steel Storage Racking System. J Earthq Eng 2020;24(3):485–505. https://doi.org/10.1080/13632469.2018.1453402.

[4] Peeters B, De Roeck G. Stochastic system identification for operational modal analysis: a review. J Dyn Syst Meas Contr 2001;123(4):659–67. https://doi.org/10.1115/1.1410370.

[5] Stochino F, Attoli A, Serra M, Napoli A, Meloni D, Mistretta F. Structural identification from operational modal analysis: the case of steel structures. Buildings 2023;13(2):548. https://doi.org/10.3390/buildings13020548.

[6] *ITU* - Infrastructure Connectivity Map. https://bbmaps.itu.int/bbmaps/ (accessed 2025-11-11).

[7] Lv B, Peng Y, Du C, Tian Y, Wu J. Review of Brillouin distributed Sensing for Structural monitoring in Transportation Infrastructure. Infrastructures 2025;10(6):148. https://doi.org/10.3390/infrastructures10060148.

[8] Hou Z, Cao D, Peng P, Ding X, Ma T, Cheng J. Analysis of Strain transfer Characteristics of Fiber Bragg Gratings for Asphalt Pavement Health monitoring. Materials 2025;18(15):3489. https://doi.org/10.3390/ma18153489.

[9] Gołdyn M, Zdanowicz K. Distributed Fiber Optic Sensing in Bridge Structural Health monitoring: Insights from Real-Life Implementations in Germany. Türkiye: Izmir; 2025.

[10] Bertulessi M, Bignami DF, Boschini I, Brunero M, Ferrario M, Menduni G, et al. Monitoring Strategic Hydraulic Infrastructures by Brillouin distributed Fiber Optic Sensors. Water 2022;14(2):188. https://doi.org/10.3390/w14020188.

[11] Barrias A, Casas J, Villalba S. Embedded distributed Optical Fiber Sensors in Reinforced Concrete Structures—A Case Study. Sensors 2018;18(4):980. https://doi.org/10.3390/s18040980.

[12] Y. Du, B. Sun, J. Li, W. Zhang, Optical Fiber Sensing and Structural Health Monitoring Technology, 2019, Springer, Singapore, doi: 10.1007/978-981-13-2865-7.

[13] Glisic B, Inaudi D. *Fibre optic methods for structural health monitoring.* Chichester, UK: John Wiley & Sons; 2007.

[14] Wang G, Song D, Pang Z, Wang F, Dai H, Li W, et al. Laser interferometry for high-speed railway health inspection using telecom fiber along the line. Nat Commun 2025;16(1):4129. https://doi.org/10.1038/s41467-025-59507-6.

[15] Bao X, Chen L. Recent progress in distributed fiber optic sensors. Sensors 2012;12(7):8601–39. https://doi.org/10.3390/s120708601.

[16] Measures RM. Structural monitoring with fiber optic technology. San Diego, CA: Academic Press; 2001.

[17] Ye XW, Su YH, Han JP. Structural health monitoring of civil infrastructure using optical fiber sensing technology: a comprehensive review. Scientific World Journal 2014;2014:652329. https://doi.org/10.1155/2014/652329.

[18] A.H. Hartog, An Introduction to Distributed Optical Fibre Sensors, 2017, CRC Press, Boca Raton, FL, doi: 10.1201/9781315119014.

[19] Zhan Z. Distributed acoustic sensing turns fiber-optic cables into sensitive seismic antennas. Seismol Res Lett 2020;91(1):1–15. https://doi.org/10.1785/0220190112.

[20] Wang Z, Lu B, Ye Q, Cai H. Recent progress in distributed fiber acoustic sensing with Φ-OTDR. Sensors 2020;20(22):6594. https://doi.org/10.3390/s20226594.

[21] Capoluongo P, Campopiano S, Cutolo A, Cusano A, Giordano M, Felli F, et al. Modal analysis and damage detection by fiber Bragg grating sensors. Sens Actuators, A 2007;133(2):415–24. https://doi.org/10.1016/j.sna.2006.04.018.

[22] Falcetelli F, Martini A, Di Sante R, Troncossi M. Strain modal testing with fiber Bragg gratings for automotive applications. Sensors 2022;22(3):946. https://doi.org/10.3390/s22030946.

[23] Cusano A, Cutolo A, Nasser J, Giordano M, Calabrò A. Dynamic strain measurements by fibre Bragg grating sensor. Sens Actuators, A 2004;110(1–3):276–81. https://doi.org/10.1016/j.sna.2003.10.031.

[24] W. Lienhart, L. Strasser, V. Dumitru, Distributed vibration monitoring of bridges with fiber optic sensing systems, in: Experimental Vibration Analysis for Civil Engineering Structures (EVACES 2023) – vol. 2, pp. 662–671, Cham: Springer, doi: 10.1007/978-3-031-39117-0_67.

[25] Benabid M-K, Baumgartner P, Jin G, Fan Y. Leakage detection using distributed acoustic sensing in gas pipelines. Sensors 2025;25(16):4937. https://doi.org/10.3390/s25164937.

[26] Ajo-Franklin JB, Dou S, Lindsey NJ, Monga I, Tracy C, Robertson M, et al. Distributed acoustic sensing using dark fiber for near-surface characterization and broadband seismic event detection. Sci Rep 2019;9:1328. https://doi.org/10.1038/s41598-018-36675-8.

[27] Culshaw B, Kersey A. Fiber-optic sensing: a historical perspective. J Lightwave Technol 2008;26(9):1064–78. https://doi.org/10.1109/JLT.0082.921915.

[28] Her S-C, Yang C-M. Dynamic strain measured by Mach–Zehnder interferometric optical fiber sensors. Sensors 2012;12(3):3314–26. https://doi.org/10.3390/s120303314.

[29] Lee BH, Kim YH, Park KS, Eom JB, Kim MJ, Rho BS, et al. Interferometric fiber optic sensors. Sensors 2012;12(3):2467–86. https://doi.org/10.3390/s120302467.

[30] Zhou H, Peng Y-P, Chen N-K. High sensitivity fiber interferometric strain sensors based on elongated fiber abrupt tapers. Micromachines 2022;13(7):1015. https://doi.org/10.3390/mi13071015.

[31] Boffi P, Ferrario M, Luch ID, Rizzelli G, Gaudino R. Optical sensing in urban areas by deployed telecommunication fiber networks. International Conference on Optical Network Design and Modeling (ONDM) 2022:1–5. 10.23919/ONDM54585.2022.9782848.

[32] Luch ID, Boffi P, Ferrario M, Rizzelli G, Gaudino R, Martinelli M. Vibration sensing for deployed metropolitan fiber infrastructure. J Lightwave Technol 2021;39(4):1204–11.

[33] Tan X, Bao Y, Zhang Q, Nassif H, Chen G. Strain transfer effect in distributed fiber optic sensors under an arbitrary field. Autom Constr 2021;124:103597. https://doi.org/10.1016/j.autcon.2021.103597.

[34] Ansari F, Libo Y. Mechanics of bond and interface shear transfer in optical fiber sensors. J Eng Mech 1998;124(4):385–94. https://doi.org/10.1061/(ASCE)0733-9399(1998)124:4(385).

[35] Dong Y, Li Q, Ansari F. Shear lag model for embedded interferometric optical fiber sensors, in Proceedings of a specialty conference on optical fiber sensors in civil engineering. Reston, VA: American Society of Civil Engineers; 2012. p. 57–73.

[36] Liu Y, Bao Y. Intelligent monitoring of spatially-distributed cracks using distributed fiber optic sensors assisted by deep learning. Measurement 2023;220:113418. https://doi.org/10.1016/j.measurement.2023.113418.

[37] Torzoni M, Manzoni A, Mariani S. A multi-fidelity surrogate model for structural health monitoring exploiting model order reduction and artificial neural networks. Mech Syst Sig Process 2023;197:110376. https://doi.org/10.1016/j.ymssp.2023.110376.

[38] Rosafalco L, Torzoni M, Manzoni A, Mariani S, Corigliano A. Online structural health monitoring by model order reduction and deep learning algorithms. Comput Struct 2021;255:106604. https://doi.org/10.1016/j.compstruc.2021.106604.

[39] Torzoni M, Rosafalco L, Manzoni A, Mariani S, Corigliano A. SHM under varying environmental conditions: an approach based on model order reduction and deep learning. Comput Struct 2022;266:106790. https://doi.org/10.1016/j.compstruc.2022.106790.

[40] Menghini A, Leander J, Castiglioni CA. A local response function approach for the stress investigation of a centenarian steel railway bridge. Eng Struct 2023;286:116116. https://doi.org/10.1016/j.engstruct.2023.116116.

[41] Menghini A, Meng B, Leander J, Castiglioni CA. Estimating bridge stress histories at remote locations from vibration sparse monitoring. Eng Struct 2024;318:118720. https://doi.org/10.1016/j.engstruct.2024.118720.

[42] Meng B, Menghini A, Leander J. Virtual sensing in steel bridges: Time series deep learning for stress prediction. Procedia Struct Integrity 2024;64:774–83. https://doi.org/10.1016/j.prostr.2024.09.342.

[43] Donadello S, Clivati C, Govoni A, Margheriti L, Vassallo M, Brenda D, et al. Seismic monitoring using the telecom fiber network. Commun Earth Environ 2024;5(1):178. https://www.nature.com/articles/s43247-024-01338-2.

[44] Ceylan H, Kanyilmaz A, Donadello S, Clivati C, Loiacono D, Herrero A, et al. Preliminary feasibility study on using fiber-optic infrastructure with an interferometric approach for structural health monitoring. In: International Conference on Experimental Vibration Analysis for Civil Engineering Structures. Switzerland: Cham: Springer Nature; 2025. p. 619–28. https://doi.org/10.1007/978-3-031-96110-6_60.

[45] H. Ceylan, A. Kanyilmaz, S. Donadello, C. Clivati, D. Loiacono, A. Herrero (Under Review). A feasibility study on the use of the deployed telecommunication fiber-optic infrastructure for structural health monitoring. J. Civil Struct. Health Monitoring.

[46] H. Ceylan, A. Kanyilmaz, S. Donadello, C. Clivati, C. Gentile, Experimental Modal Identification Using Interferometric Sensing for Dual Use of Telecom Fiber Infrastructure in Structural Health Monitoring (Preprint), 2026. (SSRN Scholarly Paper No. 6313502). Social Science Research Network, doi: 10.2139/ssrn.6313502.

[47] Bertholds A, Dandliker R. Determination of the individual strain-optic coefficients in single-mode optical fibres. J Lightwave Technol 1988;6(1):17–20. https://doi.org/10.1109/50.3956.

[48] MIDAS gen & midas FEA NX. MIDAS Information Technology Co.

[49] Zhang J, Deng Z, Xie Z, Dong Y, Li Y. Real-time strain field prediction of steel cross girder based on Proper Orthogonal Decomposition (POD) and CNN-LSTM. Internat. J. Steel Struct. 2025;1–12. https://doi.org/10.1007/s13296-025-01006-x.

[50] Rizvi SHM, Abbas M. From data to insight, enhancing structural health monitoring using physics-informed machine learning and advanced data collection methods. Eng Res Express 2023;5(3):032003. https://doi.org/10.1088/2631-8695/acefae.